A first-principles insight into thermodynamic and mechanical properties of Xonotlite and Wollastonite phases of high temperature geothermal well cement

Nguyen-Hieu Hoang [a,*], Do Tuong Ha [b], Thuat T. Trinh [c,**]

[a] Department of Materials and Nanotechnology, SINTEF Industry, Trondheim, 7034, Norway
[b] Faculty of Applied Sciences, Ton Duc Thang University, Ho Chi Minh City, 700000, Viet Nam
[c] Department of Chemistry, Norwegian University of Science and Technology - NTNU, Trondheim, 7491, Norway

ABSTRACT

This study investigates the thermodynamic and mechanical properties of two common calcium silicate phases, xonotlite ($Ca_6Si_6O_{17}(OH)_2$) and wollastonite ($CaSiO_3$), in high temperature geothermal well cement using first-principles methods. Various properties, including thermal expansion coefficients, elastic constants, free energy, and entropy, were evaluated with the use of accurate anharmonic approximations at high temperatures. The study found that wollastonite has higher mechanical strength (97 GPa) compared to xonotlite (66 GPa) and lower thermal expansion, with decreasing values at higher temperatures. Volumetric thermal expansion coefficients were also calculated at different temperatures. These results demonstrate the potential of wollastonite as a suitable material for high-temperature cement dehydration processes.

1. Introduction

Geothermal energy has been recognized as a promising renewable energy source due to its weather-independent and widely available nature, and its ability to provide a stable supply of energy [1–4]. In comparison to wind and solar energy, geothermal energy has the potential to make a significant contribution to the renewable energy mix worldwide, and particularly in the EU. However, despite its vast potential, the global contribution of geothermal energy to the total energy mix remains less than 2% [2]. This can be attributed to the high upfront costs associated with designing, drilling, and completing geothermal wells, which can constitute up to 40–50% of the total cost [2,4]. To address this issue, deep geothermal energy has emerged as a key development gateway for economically viable geothermal projects. By drilling deeper to reach high enthalpy geofluids found in superhot rocks, energy production can be increased up to 40-50MWe per well [5], which is a significant improvement over the energy output of conventional geothermal wells. Studies have shown that the energy output from three wells at 400 °C can surpass that of 42 wells at 200 °C [5,6]. However, drilling high-enthalpy geothermal wells poses several technical challenges, mainly related to the extreme high temperatures and supercritical

conditions involved [7]. These challenges must be overcome to fully realize the potential of geothermal energy as a green energy source.

The use of well cement in deep geothermal wells can result in exposure to extremely high temperatures, reaching up to 500–600 °C. At such high temperatures, the properties of the cement can be significantly altered, leading to potential failures of the wellbore and associated equipment. The common Portland cement used in well cementing is known to degrade at temperatures above 110 °C, which is commonly referred to as strength retrogression. To prevent this, silica flour is often added to the cement slurry at a rate of 30–40% by weight of cement to maintain its strength and durability [8]. However, at higher temperatures, the degradation of Portland cement becomes inevitable, and new minerals start to form, which can affect the cement's properties and behavior. In particular, the formation of tobermorite and xonotlite has been observed at high temperatures. These minerals are known to have unique mechanical and thermal properties, which make them promising candidates for high-temperature applications. Xonotlite and wollastonite are two of the main phases that are formed at temperatures ranging from 500 to 600 °C in cement systems.

The formation of xonotlite and wollastonite occurs at different temperature ranges. Xonotlite is formed at relatively lower

---

* Corresponding author.
** Corresponding author.
  E-mail addresses: hieu.nguyen.hoang@sintef.no (N.-H. Hoang), thuat.trinh@ntnu.no (T.T. Trinh).

temperatures, through the hydrothermal alteration of calcium silicate minerals such as diopside or wollastonite. In contrast, wollastonite is formed at higher temperatures through the metamorphism of calcium-rich sediments or the hydrothermal alteration of other calcium silicate minerals [9]. The precise temperature range for the formation of xonotlite and wollastonite can vary depending on factors such as pressure, the availability of reactive species, and the composition of the starting materials. Nonetheless, the formation of xonotlite and wollastonite at different temperature ranges reflects their distinct crystal structures, chemical and thermodynamic properties [10–17].

Xonotlite is a calcium silicate mineral that has a layered structure composed of Ca-polyhedra and silicate tetrahedra. The Ca-polyhedra consist of three different Ca sites, two of which are seven-coordinated by oxygen and the third is a distorted octahedron [18]. The silicate tetrahedra form a double chain, which is formed by condensation of two wollastonite chains. The Si tetrahedra can be attached to the Ca layer in two structurally equivalent ways. This results in a number of xonotlite polytypes characterized by different relative arrangements of the silicate double chain in neighboring Ca layers. The unique structural characteristics of xonotlite make it an interesting and important material for a range of industrial applications, such as in the production of cementitious materials and as a component of insulating materials for high-temperature applications.

Wollastonite $CaSiO_3$ is a member of the inosilicate group of minerals, which are characterized by the presence of chains of linked tetrahedra [19]. The crystal structure of wollastonite consists of chains of corner-sharing SiO4 tetrahedra that are connected by Ca atoms located in the channels formed between the tetrahedral chains. The unit cell of wollastonite contains two of these chains joined apex-to-apex, as well as a single SiO4 tetrahedron with one edge parallel to the chain direction in the b-axis. This results in a monoclinic crystal system with space group $P2_{1/a}$. The SiO_4 tetrahedra in wollastonite are arranged in a manner that gives the mineral a prismatic habit, with elongation along the direction of the tetrahedral chains. Additionally, the coordination of Ca in wollastonite is highly distorted, with Ca atoms coordinated to 7 or 8 oxygen atoms. The unique crystal structure and physical properties of wollastonite make it a valuable industrial mineral with applications in ceramics, construction materials, and as a source of CaO for chemical processes.

The utilization of Density Functional Theory (DFT) has emerged as a pivotal and indispensable tool in the realm of material science, particularly for the assessment of mechanical stability across a wide spectrum of materials [20–23]. This approach holds immense significance due to its capacity to provide profound insights into the structural and mechanical behavior of various materials under varying conditions. Recent research in materials science has increasingly focused on understanding the properties and behavior of C–S–H (calcium-silicate-hydrate), a key component of cementitious materials with both experimental and computational simulations [24–30]. The study of C–S–H has important implications for the durability and sustainability of concrete, as well as for the development of new cementitious materials with enhanced properties. However, there has been limited research [31] on their atomistic structure and mechanical properties at high temperature for xonotlite and wollastonite phase. The lack of chemistry and properties of Portland cement at such high temperatures are still not well understood, and further research is needed to better understand the behavior of the cement under these extreme conditions. To address this, the present study employs the density functional theory (DFT) method to investigate the structural, electronic, mechanical, and thermodynamic properties of these materials. By applying this method, we can gain insights into the behavior of xonotlite and wollastonite under high-temperature conditions, which can provide valuable information for their potential use in geothermal applications.

2. Ab-initio modelling of xonotlite and wollastonite phases

The present section outlines the methodology employed in this study to investigate the materials of interest, utilizing Density Functional Theory (DFT). DFT is a powerful computational tool widely used in material science research to accurately predict various properties of materials, such as electronic structure, bonding, and thermodynamic stability. In this study, we utilized DFT to investigate the electronic and structural properties of the materials under consideration, and to predict their behavior under different environmental conditions. The calculations were carried out using established software packages, and the chosen exchange-correlation functionals were thoroughly tested and validated for accuracy and reliability. We typically used pseudo-potentials from the GBRV pseudo-potentials library [32] and the generalized gradient approximation (GGA) in the Perdew-Burke-Ernzerhof method [33] (PBE) as implemented in the Quantum Espresso simulation package [34]. The electron valence was taken as 10e, 4e, 6e, 1e for Ca, Si, O, H atoms, respectively. After thorough convergence tests, the kinetic energy and charge density cut-offs of 60 Ry and 700 Ry were taken, respectively. This simulation approach was successfully applied to describe the mechanical properties of cement clinker [35].

Based on the size of the unit cell and total atoms of the simulation cell, **k**-points mesh was taken as (1 2 2) and (1 2 1) for xonotlite and wollastonite, respectively. Due to their large number of atoms per unit cell (60 atoms for xonotlite and 132 atoms for Wo). The structures of the two phases were plotted in 1 with VESTA package [36]. The electronic properties of the materials were investigated with the calculation of density of state (DOS) and the partial charge calculations. The PBE functional is one of the most common DFT methods in solid state calculation and was previously applied to study the properties of solid cement clinker phases [30,37]. In our work the VdW correction was added using Grimme 2D approach [38]. We denoted our method as DFT-PBE-D2. The previous work of Mai et al. [35] has shown that this DFT-PBE-D2 perform better than the Local Density Approximation (DFT-LDA). In the subsequent of this paper, the term DFT denotes the specific method DFT-PBE-D2 if not otherwise specified.

In order to evaluate the elastic properties of the clinker phases, we used the established method in the computational material outlined briefly here. The generalized Hooke's Law for a linear elastic material is written

$$\begin{bmatrix} \sigma_1 = \sigma_{xx} \\ \sigma_2 = \sigma_{yy} \\ \sigma_3 = \sigma_{zz} \\ \sigma_4 = \sigma_{yz} \\ \sigma_5 = \sigma_{xz} \\ \sigma_6 = \sigma_{xy} \end{bmatrix} = \begin{bmatrix} C_{11} & C_{12} & C_{13} & C_{14} & C_{15} & C_{16} \\ C_{21} & C_{22} & C_{23} & C_{24} & C_{25} & C_{26} \\ C_{31} & C_{32} & C_{33} & C_{34} & C_{35} & C_{36} \\ C_{41} & C_{42} & C_{43} & C_{44} & C_{45} & C_{46} \\ C_{51} & C_{52} & C_{53} & C_{54} & C_{55} & C_{56} \\ C_{61} & C_{62} & C_{63} & C_{64} & C_{65} & C_{66} \end{bmatrix} \begin{bmatrix} \epsilon_1 = \epsilon_{xx} \\ \epsilon_2 = \epsilon_{yy} \\ \epsilon_3 = \epsilon_{zz} \\ \epsilon_4 = \epsilon_{yz} \\ \epsilon_5 = \epsilon_{xz} \\ \epsilon_6 = \epsilon_{xy} \end{bmatrix} \quad (1)$$

This notation with only one subscript for the stress and strain, numbered from 1 … 6, is helpful as it allows the equations of anisotropic elasticity to be written in matrix form. The 36's C_{ij} are called the stiffnesses. The matrix of stiffnesses is called the stiffness matrix. This matrix can be inverted so that the strains are given explicitly in terms of the stresses:

$$\begin{bmatrix} \epsilon_1 \\ \epsilon_2 \\ \epsilon_3 \\ \epsilon_4 \\ \epsilon_5 \\ \epsilon_6 \end{bmatrix} = \begin{bmatrix} S_{11} & S_{12} & S_{13} & S_{14} & S_{15} & S_{16} \\ & S_{22} & S_{23} & S_{24} & S_{25} & S_{26} \\ & & S_{33} & S_{34} & S_{35} & S_{36} \\ & & & S_{44} & S_{45} & S_{46} \\ & & & & S_{55} & S_{56} \\ & & & & & S_{66} \end{bmatrix} \begin{bmatrix} \sigma_1 \\ \sigma_2 \\ \sigma_3 \\ \sigma_4 \\ \sigma_5 \\ \sigma_6 \end{bmatrix} \quad (2)$$

The elastic constants C_{ij} and constituents of the compliance tensor S_{ij} were calculated by using finite distortion of lattice and ions implemented in the external package Thermo-pw [39]. From the calculated C_{ij} and S_{ij}, the polycrystalline corresponding bulk modulus K and shear modulus G are determined using the Voigt-Reuss-Hill (VRH)

approximation, as shown in Eqs. (3) and (4). In these equations, the underscripts R and V denote Reuss and Voigt bounds, respectively.

$$
\begin{aligned}
K_R &= \frac{1}{S_{11} + S_{22} + S_{33} + 2(S_{12} + S_{23} + S_{31})} \\
K_V &= \frac{C_{11} + C_{22} + C_{33} + 2(C_{12} + C_{23} + C_{31})}{9} \\
K &= \frac{K_R + K_V}{2}
\end{aligned}
\tag{3}
$$

$$
\begin{aligned}
G_R &= \frac{15}{4(S_{11} + S_{22} + S_{33}) - 4(S_{12} + S_{23} + S_{31}) + 3(S_{44} + S_{55} + S_{66})} \\
G_V &= \frac{C_{11} + C_{22} + C_{33} - (C_{12} + C_{23} + C_{31}) + 3(C_{44} + C_{55} + C_{66})}{15} \\
G &= \frac{G_R + G_V}{2}
\end{aligned}
\tag{4}
$$

The Young's modulus, E, and Poisson's ratio, ν, for an isotropic material can be then estimated by:

$$
E = \frac{9KG}{3K + G}, \ \nu = \frac{3K - 2G}{6K + 2G}
\tag{5}
$$

The spacial dependence of mechanic properties was plotted using Elate package [40]. The thermodynamic properties such as Gibbs free energy, entropy and heat capacity were calculated with phonon calculation using the package Thermo-pw [39]. The implementation of thermal properties calculation was described the work of Palumbo et al. [41]. Due to the relatively large unit cell size, we utilized a q-points mesh of $1 \times 2 \times 2$ for the Brillouin zone integration, which was found to provide good convergence in the phonon calculations.

In the study of materials, the thermodynamic properties of a material are crucial in determining its behavior and potential applications. These properties include the heat capacity, entropy, and Helmholtz free energy, which can be calculated using various methods such as the harmonic approximation (HA) and the quasi-harmonic approximation (QHA). While the HA method can provide a good estimation of the thermodynamic properties of a material, it assumes that the lattice vibrations are harmonic, which is not always the case at high temperatures or when there is anharmonic behavior present. QHA method, on the other hand, takes into account the anharmonicity of the lattice vibrations and allows for a more accurate estimation of properties such as thermal expansion and mechanical properties at high temperatures [42, 43]. However, the QHA method is computationally more demanding than the HA method, requiring more time and computational resources. The use of QHA in our study of xonotlite and wollastonite materials was motivated by the need to accurately model their mechanical and thermodynamic properties under such extreme conditions. Specifically, we aimed to investigate the behavior of these materials in high-temperature environments, where their mechanical strength, thermal expansion, and other properties may differ significantly from those at room temperature.

We employed the QHA method to estimate volumetric thermal expansion and bulk modulus of materials as a function of temperature. In solids, atoms vibrate around their equilibrium positions, which leads to changes in the volume and lattice parameter of the material with temperature. The QHA method also accounts for the anharmonicity of the vibrational modes at higher temperatures. The volume is treated as a variable, and the free energy is minimized at each temperature to obtain the equilibrium volume and the thermal expansion coefficient as written in

$$
\alpha = \frac{1}{V} \frac{\partial V}{\partial T}
\tag{6}
$$

where V is the volume and T is the temperature. This approach has been successfully used to study the thermodynamic and mechanical

properties of a wide range of materials, including metals, semiconductors, and ceramics. To ensure a smooth deformation, we generated a set of 11 geometries for the QHA calculations using the phonopy code. In this work, the thermodynamic calculations were conducted within a temperature range up to 800 K. However, the influence of pressure was not taken into account in the scope of this study. This allowed us to accurately capture the thermal properties of the materials, which are important for understanding their behavior in various applications [24,42,43].

3. Results and discussions

3.1. Structural properties

In this study, the initial geometry of the material was acquired through experimental measurements [18,19], which provided us with a starting point for our investigation. To refine and improve upon this initial geometry, we employed the widely recognized and well-established optimization procedure, which allowed us to systematically optimize all the relevant parameters of the unit cell. In the crystal structure of xonotlite, the position of the hydrogen atom and hydrogen bonding have been shown to play a significant role, as reported in previous studies [44]. It is worth emphasizing that the orientation of the OH bond is also of utmost importance in the structure of xonotlite, and therefore, in-depth analysis of its position is essential. To this end, we have employed the same methodology as used in the previous study to adjust the position of the OH bond in our DFT calculations. By implementing this optimization process, we were able to obtain a highly optimized structure that is representative of the material under investigation. As illustrated in Fig. 1, the optimized structure we derived from this approach exhibits a marked improvement in terms of its structural integrity and stability, as well as its overall physical and chemical properties. The optimized structure features a highly ordered and well-defined arrangement of atoms, which indicates a high degree of crystalline order and a lower likelihood of defects or impurities in the material.

The structural properties of xonotlite and wollastonite, including lattice parameters and angles, are presented in Table 1 and Table 2. The optimization results from DFT calculations demonstrated excellent agreement with experimental data, with a deviation of less than 1% from the expected values. The close match between the computational and experimental data indicates the reliability of the DFT method for predicting structural properties of xonotlite Additionally, the accuracy of the DFT method in reproducing the experimental lattice parameters and angles for xonotlite suggests its potential for predicting other structural properties of materials.

3.2. Mechanic properties

This section presents a comprehensive comparison of the numerical elastic properties of the xonotlite and wollastonite phases obtained from our DFT calculations with those reported in the literature. However, it should be noted that in some of the experimental studies, Poisson's ratio was not determined directly, but rather an assumed value was used. This may introduce some degree of uncertainty in the reported values and should be taken into account when interpreting the results. The corresponding bulk and shear moduli, K and G are also provided, using the following equation with an assumed Poisson's ratio of 0.3:

$$
K = \frac{E}{3(1 - 2\nu)}, \ G = \frac{E}{2(1 + \nu)}
\tag{7}
$$

Table 3 provides a comprehensive summary of all the calculated elastic constants C_{ij} for the xonotlite structure. Our analysis reveals that the values of C_{11}, C_{22}, and C_{33} are comparable with each other, and fall within the range of 100–171 GPa, indicating that the material possesses similar levels of stiffness in these directions. However, the material is
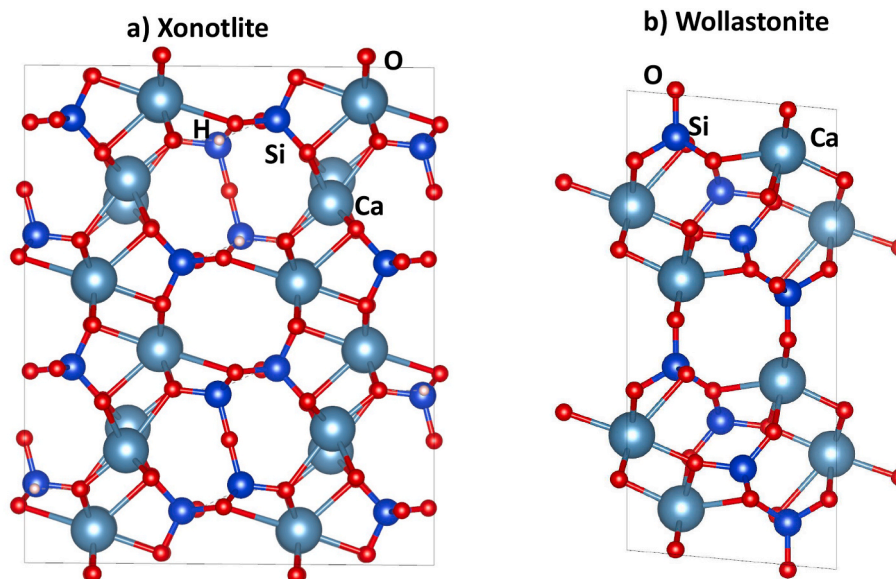
a) Xonotlite

b) Wollastonite

Fig. 1. Optimized crystal structure DFT-PBE-D2 calculation: xonotlite (a), wollastonite (b). See the text for more details.

Table 1
Comparasion between theoretical calculated crystall parameters and experimental values for the xonotlite unit cell.

Parameter	DFT_PBE_D2 (this work)	Experimental [18]	Relative deviation (%)
a	17.023	17.032	0.1%
b	7.377	7.363	−0.2%
c	14.066	14.023	−0.3%
α	90.00	90.00	0.0%
β	90.54	90.36	−0.2%
γ	90.00	90.00	0.0%

Table 2
Comparasion between theoretical calculated crystall parameters and experimental values for the wollastonite unit cell.

Parameter	DFT_PBE_D2 (this work)	Experimental [19]	Relative deviation (%)
A	15.407	15.424	0.1%
B	7.359	7.324	−0.5%
C	7.076	7.069	−0.1%
A	90.00	90.00	0.0%
B	94.79	95.37	0.6%
Γ	90.00	90.00	0.0%

Table 3
Calculated elastic constants C_{ij} (GPa) of xonotlite See eq. (1) for more details on the direction of i,j notation.

C_{ij}	1	2	3	4	5	6
1	132.1	40.3	26.7	0.0	−4.1	0.0
2	40.3	171.0	38.2	0.0	5.9	0.0
3	26.7	38.2	100.5	0.0	13.3	0.0
4	0.0	0.0	0.0	49.6	0.0	−2.4
5	−4.1	5.9	13.3	0.0	33.6	0.0
6	0.0	0.0	0.0	−2.4	0.0	45.8

expected to be less compressive in the second direction, as evidenced by the highest value of C_{22} compared to those of C_{11} and C_{33}. Moreover, the xonotlite material exhibits a high shear resistance along the first direction, with the highest shear modulus C_{44} when compared to C_{55} and C_{66}. This high shear resistance is attributed to the anisotropic nature of the

material, which is reflected in the directional elastic moduli plot shown in Fig. 3. As seen in this figure, the elastic moduli exhibit marked directional dependence, with significant variations observed between the different directions. This anisotropic behavior arises from the inherent structural asymmetry of the material, which affects its mechanical response under different loading conditions. It is worth noting that the anisotropy of the material may have significant implications for its practical applications, particularly in the design of structural materials and devices. The directional dependence of the elastic properties can affect the overall strength and stiffness of the material, and may also influence its fracture behavior and resistance to deformation. Therefore, a thorough understanding of the elastic properties of anisotropic materials like xonotlite is crucial for their successful implementation in various engineering and scientific applications.

Table 4 provides a detailed summary of all the calculated elastic constants C_{ij} of the wollastonite phase. Our analysis reveals that the elastic moduli of wollastonite are slightly higher than those of xonotlite Specifically, the values of C_{11}, C_{22}, and C_{33} fall within the range of 158–189 GPa, which is higher than the corresponding values for xonotlite Similar to Xo, the wollastonite phase is expected to exhibit less compressibility in the second direction, as indicated by the higher value of C_{22} in comparison to those of C_{11} and C_{33}. Moreover, the shear resistance of the wollastonite phase exhibits a similar behavior as that of Xo, with higher shear resistance observed along the first direction. This is evident from the more pronounced value of C_{44} when compared to C_{55} and C_{66}. As with Xo, the anisotropic nature of wollastonite is also apparent, although to a lesser extent. Fig. 2 illustrates this point by showing slight variations in the directional elastic moduli of the material.

The observed differences in the elastic properties of the xonotlite and wollastonite phases can be attributed to variations in their crystal

Table 4
Calculated elastic constants C_{ij} (GPa) of wollastonite See eq. (1) for more details on the direction of i,j notation.

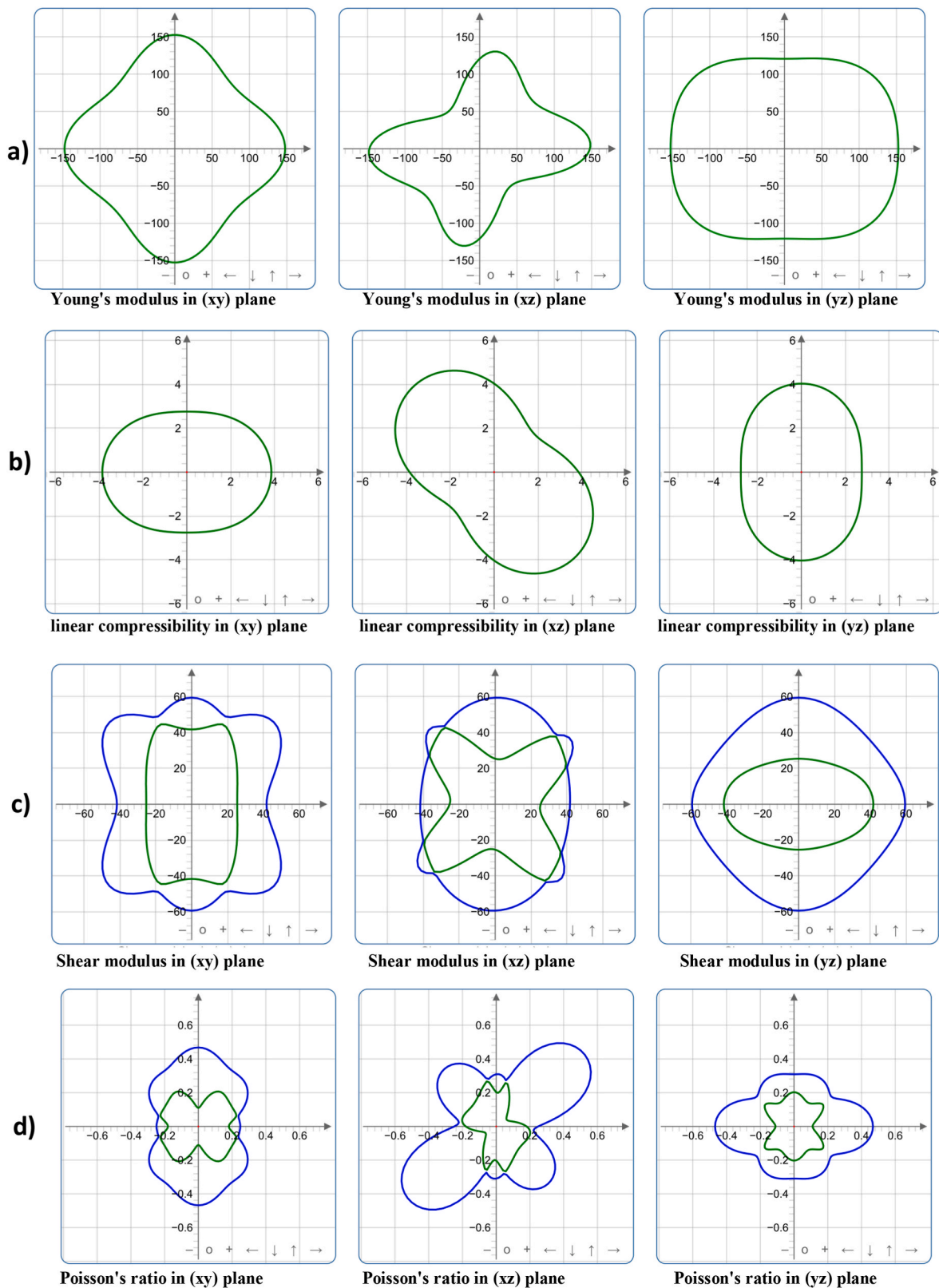| C_{ij}	1	2	3	4	5	6
1	170.4	50.8	53.4	0.0	6.7	0.0
2	50.8	188.7	67.5	0.0	−1.3	0.0
3	53.4	67.5	158.0	0.0	13.7	0.0
4	0.0	0.0	0.0	58.8	0.0	0.8
5	6.7	−1.3	13.7	0.0	27.1	0.0
6	0.0	0.0	0.0	0.8	0.0	41.8

Fig. 2. Spatial dependence of (a) Young's modulus, (b) linear compressibility, (c) shear modulus, and (d) Poisson's ratio of wollastonite.

structures and atomic arrangements. The differences in the elastic properties of the two phases may have important implications for their potential applications in various fields, including materials science, engineering, and nanotechnology. Our analysis of the elastic properties of the wollastonite phase reveals higher elastic moduli than those of Xo,

indicating greater stiffness in this phase. Similar to Xo, the wollastonite phase exhibits directional dependence in its elastic properties, with higher shear resistance along the first direction. The observed anisotropy of the material may have important implications for its potential applications in various fields, and underscores the importance of a
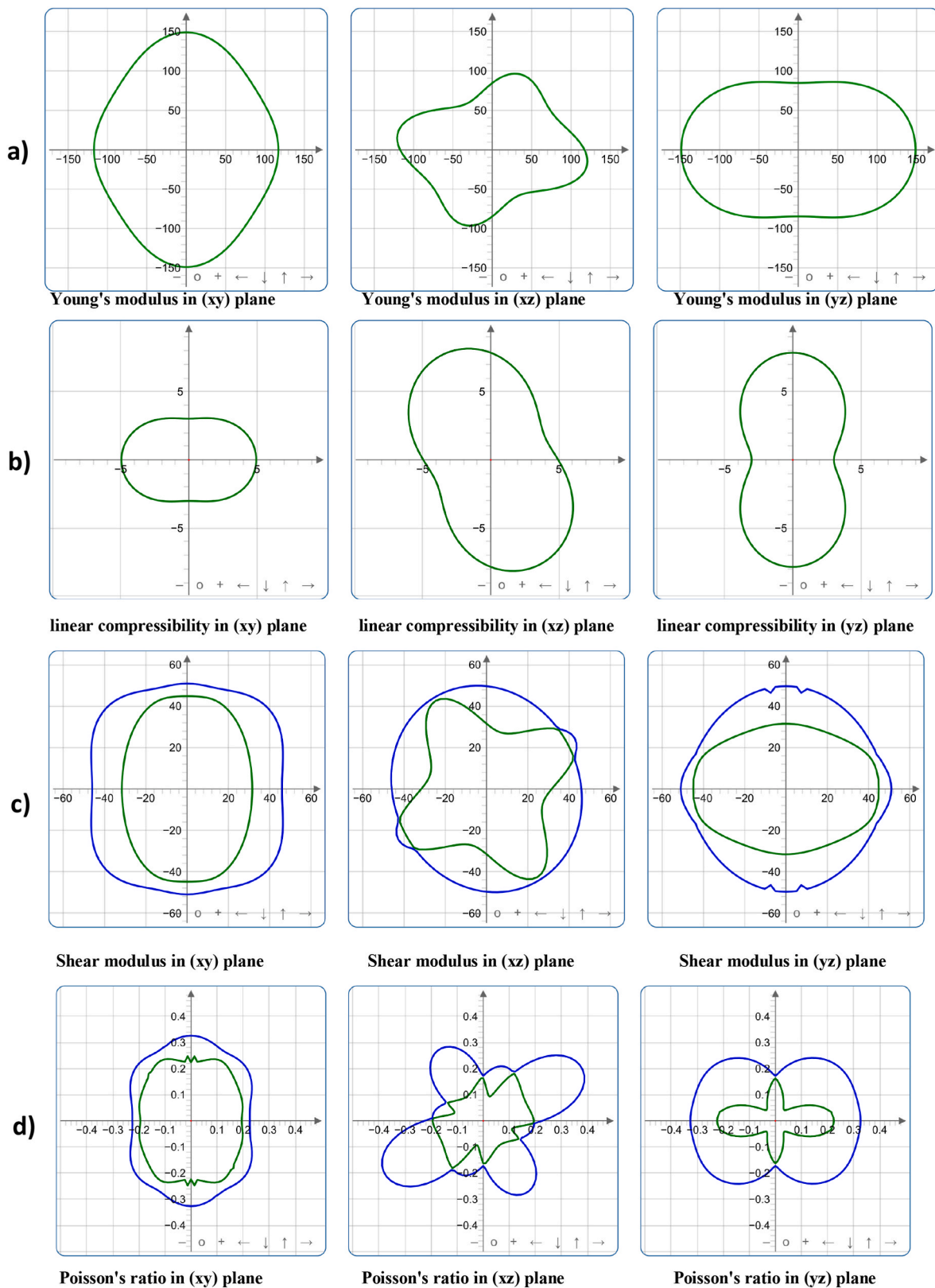
Fig. 3. Spatial dependence of (a) Young's modulus, (b) linear compressibility, (c) shear modulus, and (d) Poisson's ratio of xonotlite.

thorough understanding of its elastic properties.

We present a comparison between the experimental and numerical elastic properties of the xonotlite and wollastonite structures, which were evaluated using the RVH method. The summary of the obtained results is provided in Table 5. It is evident from the table that the Bulk

modulus of wollastonite is approximately 30% lower than that of Xo, while the shear and Young's moduli are similar for both materials. To assess the reliability of our numerical results, we also compared them with the available experimental data from the literature. To the best of our knowledge, there are no documented mechanical properties for

Table 5
Calculated mechanic properties of bulk modulus K (GPa), young's modulus E (GPa), shear modules G (GPa), and Poisson ration for xonotlite and wollastonite.

Phase	K	E	G	v
Xonotlite				
DFT (this work)	66	108	44	0.23
Experimental	/	/	/	/
Wollastonite				
DFT (this work)	94	118	46	0.29
Experimental [45]	102	129	50	0.23

xonotlite in the literature. The results of this comparison indicate that the calculated values for wollastonite are in good agreement with the experimental data. Specifically, our calculations slightly underestimate the experimental data, with the largest discrepancy being around 10% of the experimental values. These findings demonstrate the accuracy and reliability of our numerical methods, which can be used to predict the mechanical properties of materials with a high degree of confidence.

3.3. Electronic property

In this section, we aimed to investigate the electronic structure of xonotlite by analyzing the contribution of each atom type (Ca, Si, O, and H) to the total density of states (DOS). In all our calculations, we set the energy of the Fermi level relatively to zero. The results of our analysis are presented in Fig. 4, where we observe that both Oxygen and Calcium atoms contribute to the valence region of the DOS. In contrast, the conductive region is dominated by Calcium atoms, with a relatively low contribution from Oxygen atoms. Moreover, we found that Si and H atoms make a negligible contribution to the total DOS. Our calculated band-gap of xonotlite is found to be 4.6 eV. This value indicates that xonotlite is an indirect band-gap material, where the highest occupied state and the lowest unoccupied state are located at different points in the Brillouin zone. These findings provide valuable insights into the electronic properties of xonotlite and can aid in the design and development of materials with desired electronic properties.

Similarly, we examined the electronic structure of wollastonite by investigating the contribution of each atom type (Ca, Si, and O) to the total density of states (DOS). Fig. 5 presents the calculated DOS plot, and it shows that both Oxygen and Calcium atoms contribute to the valence
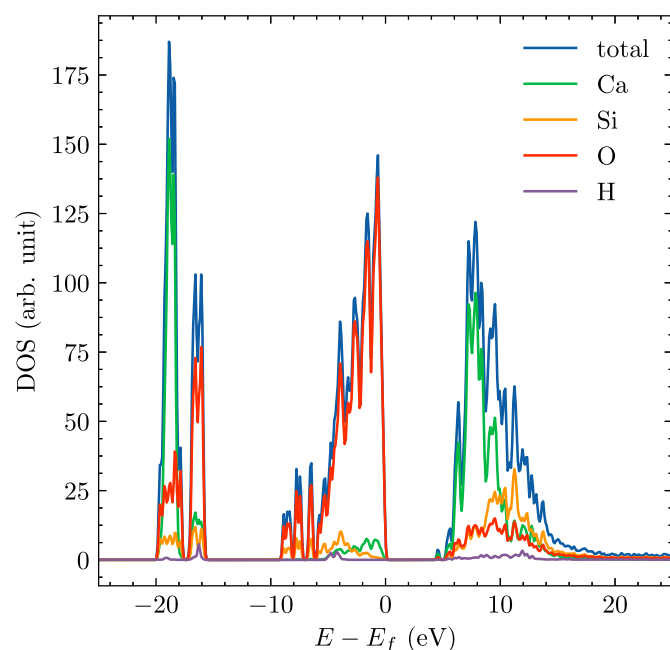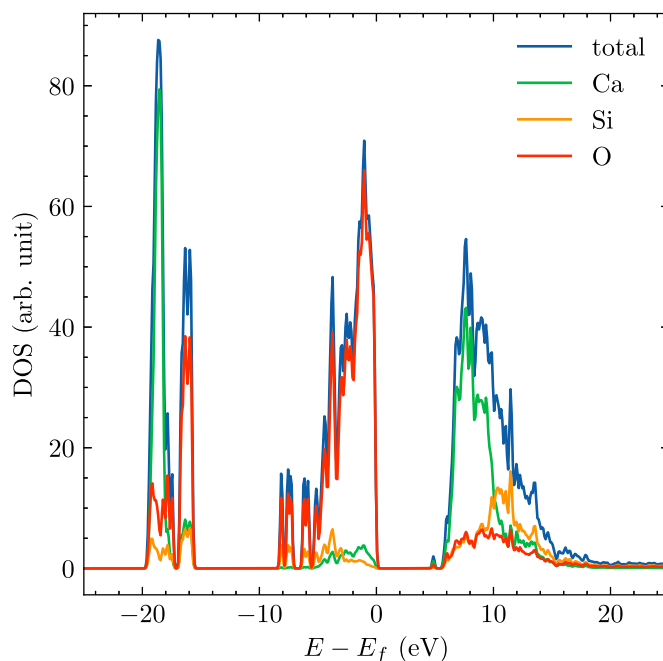

Fig. 5. Total Density of State of wollastonite with atomic contributions.

region, while the conductive region is dominated by Calcium atoms with a low contribution from Oxygen. Silicon atoms make only a small contribution to the total DOS. Unlike in xonotlite, there is no H atom present in this structure.

The DFT calculated band-gap values of xonotlite and wollastonite are 4.72 eV and 4.97 eV, respectively. These values are in consistent with calculated values of other calcium silicate structures, such as C_2S and C_3S phases, which typically fall within the range of 3.4–5.81 eV [27,30, 35,46]. This is not surprising, given that these materials are commonly classified as electrical insulators. However, it should be noted that the electronic properties of these materials can be altered in the presence of defects or heterogeneities in the structure. For instance, impurities or defects may introduce energy states within the band gap, thereby altering the electrical conductivity and other electronic properties of the material.

3.4. Thermodynamics properties

The thermodynamic properties of materials are important in understanding their behavior at different temperatures, particularly in high-temperature applications. In this study, we used the DFT-PBE-D2 method to calculate various thermodynamic parameters of the calcium silicate phases xonotlite and wollastonite over a temperature range of 0K–800K. The calculated parameters included free energy, entropy, and heat capacity at constant volume (C_v). The calculated thermodynamic profiles of xonotlite and wollastonite are depicted in Fig. 6. It is worth noting that the free energy decreases with increasing temperature, while entropy and thermal capacity increase. The observed profiles of xonotlite and wollastonite are similar, but the values of xonotlite are approximately six times higher than those of wollastonite This is due to the fact that the number of atoms per mole of xonotlite ($Ca_6Si_6O_{17}(OH)_2$) is six times higher than that of wollastonite ($CaSiO_3$). As a result, the entropy and heat capacity of xonotlite are expected to be greater than wollastonite as is shown in Fig. 6.

To verify the accuracy of our calculations, we compared the experimental values of the entropy and heat capacity of wollastonite at T = 298 K with our calculated values. Unfortunately, the thermochemical properties of xonotlite have not been reported in the literature to date. Our DFT-PBE-D2 method yielded the values of 99 J/mol/K and 105 J/
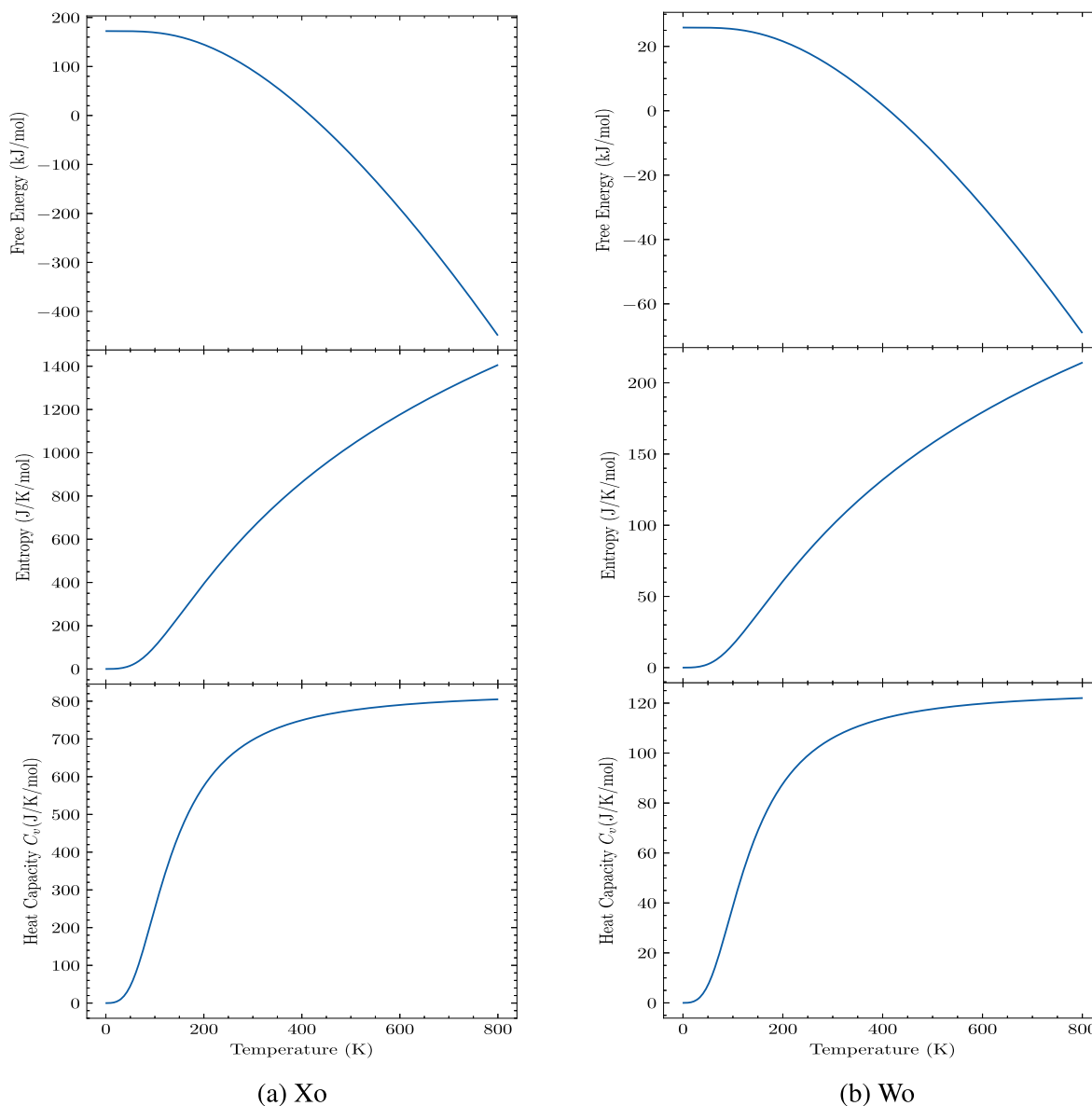

Fig. 4. Total Density of State of xonotlite with atomic contributions.

(a) Xo

(b) Wo

Fig. 6. Calculated thermodynamic properties (free energy, entropy and heat capacity) of xonotlite and wollastonite phases for the temperature range of 0K–800K.

mol/K for the entropy and heat capacity of wollastonite, respectively. These values are in good agreement with the experimental values, as shown in Table 6. This confirms the reliability of our method in predicting the thermodynamic properties of calcium silicate structures. It is worth noting that the heat capacity at constant volume C_v was calculated in the DFT calculation. However, for solid structures, the C_v value is almost the same as the heat capacity at constant pressure C_p. Hence, we can directly compare our calculated C_v with the experimental C_p value. The agreement between our theoretical calculations and experimental results was excellent, with a difference of less than 15%. These findings further validate the DFT-PBE-D2 method's accuracy and suitability for studying the thermodynamic properties of calcium silicate structures at

Table 6
Thermochemical properties (J/K/mol) for xonotlite and wollastonite at reference temperature 298K

Phase	Entropy	Heat capacity
Xonotlite DFT (this work)	650	696
Wollastonite DFT (this work)	99	105
Wollastonite Exp [47].	82	86

different temperatures.

3.5. Effect of temperature on mechanical properties

The Helmholtz free energy of xonotlite is calculated for various temperatures and volumes, as shown in Fig. 7 (a). The equilibrium volume at each temperature is obtained by identifying the minimum Helmholtz free energy, and this data is then used to construct a plot of equilibrium volume as a function of temperature, as shown in Fig. 7 (b). The volumetric thermal expansion coefficient can be calculated from this data using equation (6) and plotted in Fig. 7 (c). The variations of the Bulk modulus of xonotlite at high temperature is depicted in Fig. 7 (d). A similar plot for wollastonite is presented in Fig. 8. Our results show that the trend in the bulk modulus for both materials is consistent between QHA and finite distortion calculations that wollastonite exhibits much higher mechanical strength than xonotlite. Remarkably, our results indicate that the bulk modulus values obtained using the QHA method (see Table 7) are in excellent agreement with those calculated using finite distortion of lattice and ions approximation (see Table 5). The difference between the bulk modulus values obtained using these
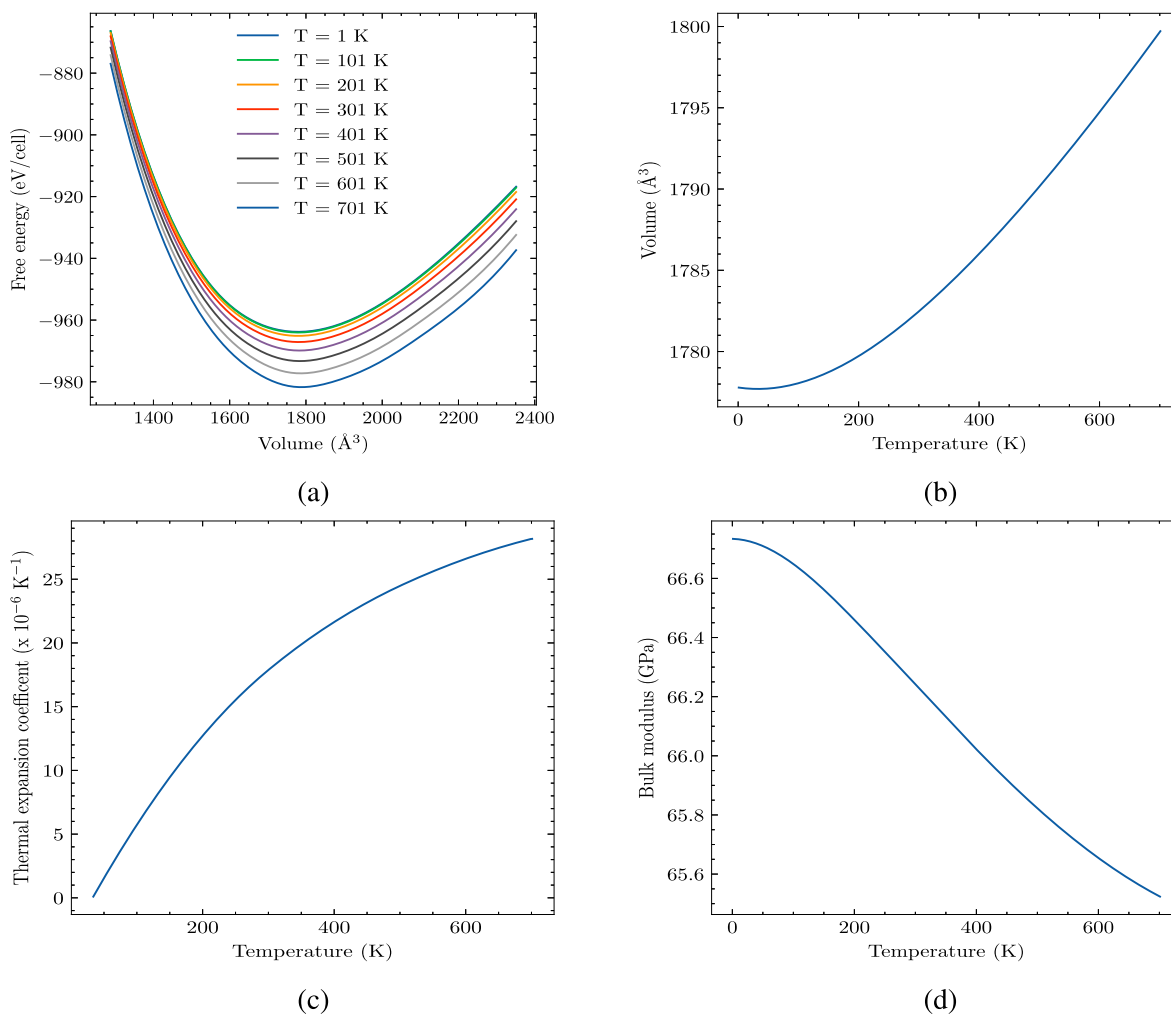
Fig. 7. Calculated properties of xonotlite structure using quasi harmonic approximation and DFT-PBE-D2 method. (a) Dependence of free energy on the volume at different temperatures. (b) Temperature dependence of the unit cell volume. (c) Temperature dependence of the volummetric thermal expansion coefficient. (d) Temperature dependence of the bulk modulus.

two methods is less than 5%. Moreover, comparison with experimental data reveals a slight improvement in the bulk modulus calculated by QHA method. These findings suggest that the QHA method is a reliable and accurate approach for predicting the bulk modulus of wollastonite.

The results presented in Table 7 demonstrate the influence of temperature on the volumetric thermal expansion and Bulk modulus of the two phases under investigation. The volumetric thermal expansion of both phases shows a substantial increase with temperature, consistent with previous experimental observations. Notably, the volumetric thermal expansion increases by approximately 90% over the range of temperatures from room temperature to 700K. In contrast, the Bulk modulus of the materials experiences only a minor decrease, with a change of less than 2% observed over the same temperature range. These findings suggest that temperature has a more significant impact on the volumetric thermal expansion than on the Bulk modulus of these materials.

4. Concluding remarks

This study employs ab-initio atomistic simulations based on DFT using the PBE-D2 functional to investigate the mechanical, electronic, and thermodynamical properties of xonotlite and wollastonite materials. Additionally, the effects of temperature on these properties were studied. The obtained results have led to several significant conclusions, which include:

- The consistency between the theoretical and experimental values of mechanical properties and lattice constants suggests that the DFT-PBE-D2 method is the preferred approach for modeling and predicting the properties of calcium silicate structures. It also indicates that the structure of xonotlite and wollastonite can be effectively described by the DFT-PBE-D2 method, and provides confidence in the accuracy of the calculated properties. The results also suggest that the use of QHA can enhance the accuracy of predictions for the properties of calcium silicate minerals at high temperatures, which is of great importance for their application in high-temperature processes.

- The results show that the calculated elastic moduli values of both materials are in good agreement with the available experimental data. Both materials exhibit highly anisotropic behavior, as evidenced by the significant differences in elastic properties along different crystallographic directions. It was observed that the materials are expected to have lower compressive strength in the second direction, which is consistent with the anisotropic behavior of the materials.

- The electronic properties of materials play a crucial role in determining their potential applications. We obtained the band gap values of 4.72 eV and 4.97 eV for xonotlite and wollastonite, respectively. These values are consistent with those reported for other calcium silicate structures and suggest that these materials are electrically insulating in nature. However, it is important to note that the
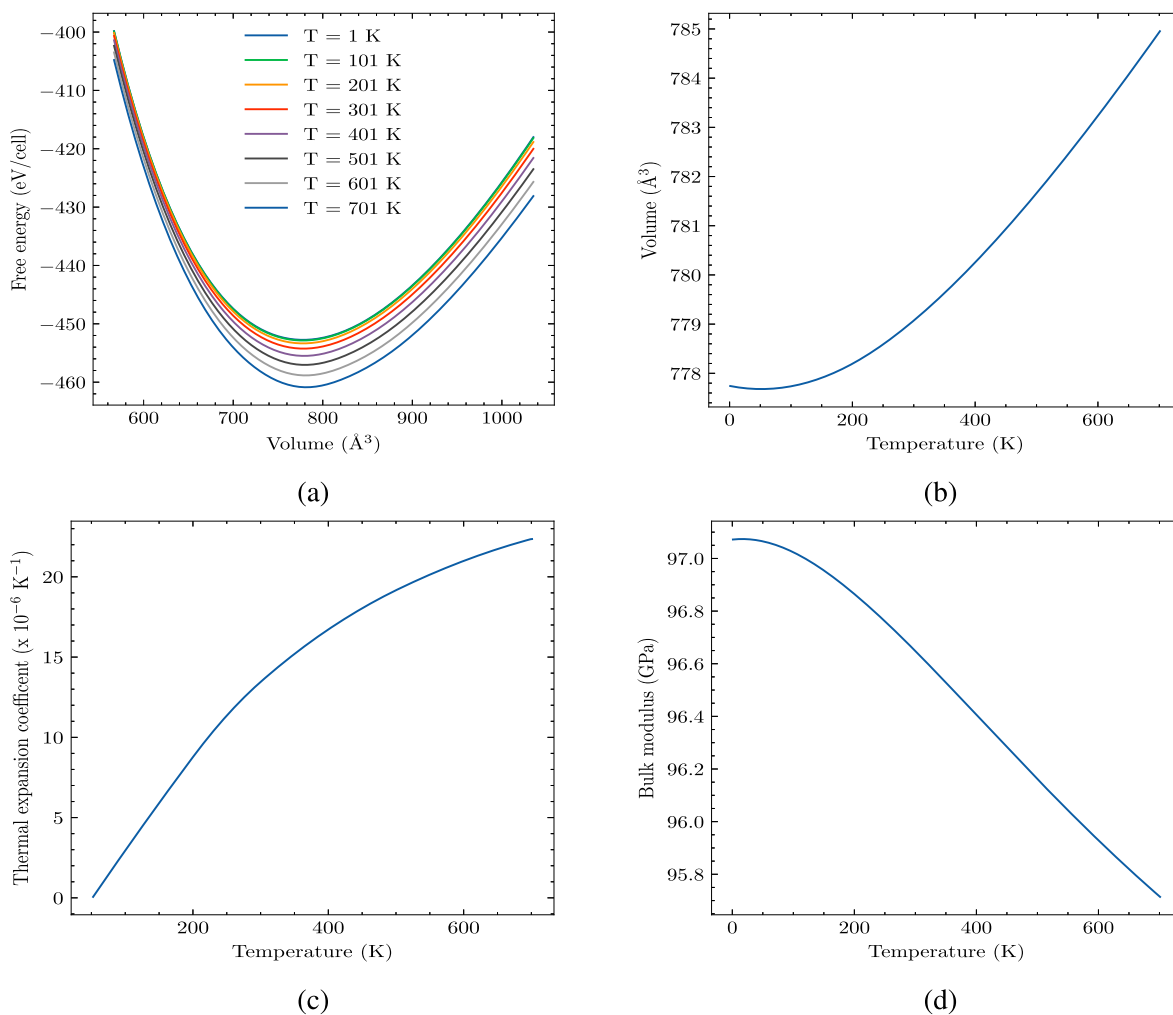
Fig. 8. Calculated properties of wollastonite structure using quasi harmonic approximation and DFT-PBE-D2 method. (a) Dependence of free energy on the volume at different temperatures. (b) Temperature dependence of the unit cell volume. (c) Temperature dependence of the volummetric thermal expansion coefficient. (d) Temperature dependence of the bulk modulus.

Table 7
Calculated volumetric thermal expansion coefficient and Bulk modulus by DFT-PBE-D2 method for xonotlite and wollastonite at high temperature by QHA method.

Phase	Temperature (K)	α (10^{-6} K^{-1})	K (GPa)
Xonotlite	298	16	66.3
	700	28	65.5
Wollastonite	298	13	96.7
	700	22	95.7

presence of defects or heterogenous atoms in the structure may significantly alter the electronic properties of these materials. Further investigations are necessary to fully understand the electronic behavior of these materials and their potential applications.

● The results of our calculations reveal that both xonotlite and wollastonite exhibit a decreasing trend in their Bulk modulus with increasing temperature. However, this decrease is only around 2% when the temperature is raised from room temperature to 700K. Furthermore, we find that wollastonite exhibits significantly higher mechanical strength compared to xonotlite. These findings could have important implications for the selection and design of materials for high-temperature applications where mechanical strength is a crucial factor.

● In conclusion, this study provides significant insights into the fundamental properties of xonotlite and wollastonite materials, which can aid in their development and application in various fields. The findings from this study can serve as a basis for future investigations on the optimization and modification of these materials for specific industrial and technological applications. However, it should be acknowledged that the observed decline in cement performance under high-temperature environments has not been comprehensively elucidated within the scope of this study. Subsequent investigations could also focus on making strategies to mitigate this decline and thoroughly exploring the potential applications and efficacy of wollastonite in high-temperature cement scenarios.

Credit author statement

Nguyen-Hieu Hoang: Writing – original draft, Investigation, Validation, Writing, Software, Editing, Funding acquisition. Do Tuong Ha: Investigation, Validation, Editing. Thuat T. Trinh: Conceptualization, Validation, Supervision, Resources, Writing – review & editing.

Declaration of competing interest

The authors declare that they have no known competing financial interests or personal relationships that could have appeared to influence the work reported in this paper.

Data availability

Data will be made available on request.

Acknowledgements

References

[1] K. Weber, S. Vedula, Geothermal energy: a review on the sustainability, greenhouse gas emission, and prospects for India, Renewable Sustainable Energy Rev. 71 (2017) 768–779, https://doi.org/10.1016/j.rser.2016.12.121.

[2] A. Beck, J.W. Lund, World geothermal power generation 2005–2012, Renewable Sustainable Energy Rev. 26 (2013) 317–323, https://doi.org/10.1016/j.rser.2013.05.007.

[3] D. Kale, Geothermal energy, Proc. Indian Natl. Sci. Acad. 81 (4) (2015) 27–34, https://doi.org/10.16943/ptinsa/2015/v81i4/48307.

[4] E. Rodrigues, M.S. Fernandes, l. Gomes, A.R. Gaspar, J.J. Costa, Performance-based design of multi-story buildings for a sustainable urban environment: a case study, Renewable Sustainable Energy Rev. 113 (2019), 109243, https://doi.org/10.1016/j.rser.2019.109243.

[5] W.E. Glassley, Geothermal Energy: Renewable Energy and the Environment, CRC Press, 2014, https://doi.org/10.1201/b16611.

[6] T. Yin, Q. Li, X. Li, Experimental investigation on mode i fracture characteristics of granite after cyclic heating and cooling treatments, Eng. Fract. Mech. 222 (2019), 106740, https://doi.org/10.1016/j.engfracmech.2019.106740.

[7] G. Gruben, B. Dillingh, G.S. Kaldal, N.-H. Hoang, J. Wollenweber, G. Rrvik, I. Thorbjornsson, B. Nyhus, Thermo-mechanical tensile testing of geothermal casing materials, Geothermics 89 (2021), 101944, https://doi.org/10.1016/j.geothermics.2020.101944.

[8] E. Nelson, D. Guillot, in: Well Cementing, second ed., 2006, pp. 258–263. Schlumberger, Sugar Land, TX 77478.

[9] I.G. Richardson, The calcium silicate hydrates, Cement Concr. Res. 38 (2) (2008) 137–158.

[10] R.M. Wentzcovitch, N.L. Ross, G. Price, Ab initio study of MgSiO3 and CaSiO3 perovskites at lower-mantle pressures, Phys. Earth Planet. In. 90 (1–2) (1995) 101–112, https://doi.org/10.1016/0031-9201(94)03001-y.

[11] T. Gasparik, K. Wolf, C. Smith, Experimental determination of phase relations in the CaSiO3 system from 8 to 15 GPa, Am. Mineral. 79 (11–12) (1994) 1219–1222.

[12] H. Tamai, T. Yagi, High-pressure and high-temperature phase relations in CaSiO3 and CaMgSi2O6 and elasticity of perovskite-type CaSiO3, Phys. Earth Planet. In. 54 (3–4) (1989) 370–377, https://doi.org/10.1016/0031-9201(89)90254-9.

[13] E. Essene, High-pressure transformations in CaSiO3, Contrib. Mineral. Petrol. 45 (3) (1974) 247–250, https://doi.org/10.1007/bf00383442.

[14] W.-L. Huang, P. Wyllie, Melting and subsolidus phase relationships for CaSiO3 to 35 kilobars pressure, Am. Mineral. 60 (3–4) (1975) 213–217.

[15] R. Hemley, M. Jackson, R. Gordon, Theoretical study of the structure, lattice dynamics, and equations of state of perovskite-type MgSiO3 and CaSiO3, Phys. Chem. Miner. 14 (1) (1987) 2–12, https://doi.org/10.1007/bf00311142.

[16] V. Swamy, L.S. Dubrovinsky, Thermodynamic data for the phases in the CaSiO3 system, Geochem. Cosmochim. Acta 61 (6) (1997) 1181–1191, https://doi.org/10.1016/s0016-7037(96)00403-6.

[17] P. Richet, R.A. Robie, B.S. Hemingway, Thermodynamic properties of wollastonite, pseudowollastonite and CaSiO3 glass and liquid, ejm 3 (3) (1991) 475–484, https://doi.org/10.1127/ejm/3/3/0475.

[18] C. Hejny, T. Armbruster, Polytypism in xonotlite Ca6Si6O17(OH)2</sub> Z. für Kristallogr. - Cryst. Mater. 216 (7) (2001) 396–408, https://doi.org/10.1524/zkri.216.7.396.20363.

[19] Y. Ohashi, Polysynthetically-twinned structures of enstatite and wollastonite, Phys. Chem. Miner. 10 (5) (1984) 217–229, https://doi.org/10.1007/bf00309314.

[20] Y. Cao, T. Li, Y. Xu, P. Wang, J. Liu, D. Zhang, J. Duan, S. Zhou, Theoretical predictions of stability, electronic properties, elastic anisotropy, thermodynamics, and optical properties of mb2 (m= v, nb, zr), J. Mater. Sci. 57 (7) (2022) 4605–4624.

[21] Y. Cao, Q. Lin, Q. Huang, Q. Xu, S. Zhou, First-principles predictions of corrosion resistance of (0001) surface of co and co3x (x= cr, ni, mn) compounds, Comput. Theor. Chem. 1225 (2023), 114171.

[22] Y. Cao, Q. Huang, Q. Lin, Y. Xu, S. Zhou, First-principles calculations to study the effect of pressure on the structural and elastic properties of sc3tc4 (t= ni, os, ru), Solid State Commun. 369 (2023), 115195.

[23] Q. Lin, Q. Huang, Y. Xu, Y. Cao, The mechanical, thermodynamic and electronic properties of tm2crb2 borides with tm= v, nb, ta: a first-principles predictions, Solid State Commun. 368 (2023), 115184.

[24] A. Togo, L. Chaput, I. Tanaka, G. Hug, First-principles phonon calculations of thermal expansion in ti 3 SiC 2, ti 3 AlC 2, and ti 3 GeC 2, Phys. Rev. B 81 (17) (2010), 174301.

[25] G. Zhang, D. Long, W. Xu, X. Cheng, S. Huang, C. Zhang, M. Zhou, K. Mei, L. Zhang, Elucidating the mechanical property-enhancement mechanism of ferrite in oil-well cement using spherical ferrite, Cement Concr. Res. 161 (2022), 106950, https://doi.org/10.1016/j.cemconres.2022.106950.

[26] G. Zhang, Z. Wu, X. Cheng, X. Sun, C. Zhang, M. Zhou, Mechanical properties of high-ferrite oil-well cement used in shale gas horizontal wells under various loads, Construct. Build. Mater. 319 (2022), 126067, https://doi.org/10.1016/j.conbuildmat.2021.126067.

[27] H.-J. Hou, W.-X. Chen, H.-J. Zhu, X.-W. Lu, S.-R. Zhang, Q.-F. Zhang, Analysis of the structural, elastic constants, electronic, optical, dynamical, and thermodynamic in dicalcium silicate with various pressures, Vacuum 210 (2023), 111869, https://doi.org/10.1016/j.vacuum.2023.111869.

[28] C. Qi, X. Xu, D. Wang, Y. Feng, Q. Zhang, Q. Chen, Coverage-dependent adsorption of H2O on dicalcium silicate (1 0 0) surface: a DFT study, Construct. Build. Mater. 321 (2022), 126403, https://doi.org/10.1016/j.conbuildmat.2022.126403.

[29] J. Zhu, Q. Wu, X. Guan, R. Zhao, Substitution preference of chromium ions in the clinker phase of ordinary Portland cement, New J. Chem. 47 (2) (2023) 563–570, https://doi.org/10.1039/d2nj04905h.

[30] M. Laanaiya, A. Bouibes, A. Zaoui, Understanding why alite is responsible of the main mechanical characteristics in Portland cement, Cement Concr. Res. 126 (2019), 105916, https://doi.org/10.1016/j.cemconres.2019.105916.

[31] S.J. Edrees, M.M. Shukur, M.M. Obeid, First-principle analysis of the structural, mechanical, optical and electronic properties of wollastonite monoclinic polymorph, Comput. Condens. Matter 14 (2018) 20–26, https://doi.org/10.1016/j.cocom.2017.12.004.

[32] K.F. Garrity, J.W. Bennett, K.M. Rabe, D. Vanderbilt, Pseudopotentials for high-throughput DFT calculations, Comput. Mater. Sci. 81 (2014) 446–452, https://doi.org/10.1016/j.commatsci.2013.08.053.

[33] J.P. Perdew, K. Burke, M. Ernzerhof, Generalized gradient approximation made simple, Phys. Rev. Lett. 77 (18) (1996) 3865–3868, https://doi.org/10.1103/physrevlett.77.3865.

[34] P. Giannozzi, S. Baroni, N. Bonini, M. Calandra, R. Car, C. Cavazzoni, D. Ceresoli, G.L. Chiarotti, M. Cococcioni, I. Dabo, A. Dal Corso, S. de Gironcoli, S. Fabris, G. Fratesi, R. Gebauer, U. Gerstmann, C. Gougoussis, A. Kokalj, M. Lazzeri, L. Martin-Samos, N. Marzari, F. Mauri, R. Mazzarello, S. Paolini, A. Pasquarello, L. Paulatto, C. Sbraccia, S. Scandolo, G. Sclauzero, A.P. Seitsonen, A. Smogunov, P. Umari, R.M. Wentzcovitch, Quantum espresso: a modular and open-source software project for quantum simulations of materials, J. Phys. Condens. Matter 21 (39) (2009), 395502, https://doi.org/10.1088/0953-8984/21/39/395502.

[35] N.L. Mai, N.-H. Hoang, H.T. Do, M. Pilz, T.T. Trinh, Elastic and thermodynamic properties of the major clinker phases of Portland cement: insights from first principles calculations, Construct. Build. Mater. 287 (2021), 122873, https://doi.org/10.1016/j.conbuildmat.2021.122873.

[36] K. Momma, F. Izumi, VESTA 3 for three-dimensional visualization of crystal, volumetric and morphology data, J. Appl. Crystallogr. 44 (6) (2011) 1272–1276, https://doi.org/10.1107/s0021889811038970.

[37] H. Manzano, E. Durgun, M.J. Abdolhosseine Qomi, F.-J. Ulm, R. Pellenq, J. Grossman, Impact of chemical impurities on the crystalline cement clinker phases determined by atomistic simulations, Cryst. Growth Des. 11 (7) (2011) 2964–2972, https://doi.org/10.1021/cg200212c.

[38] S. Grimme, J. Antony, S. Ehrlich, H. Krieg, A consistent and accurate ab initio parametrization of density functional dispersion correction (DFT-d) for the 94 elements h-Pu, J. Chem. Phys. 132 (15) (2010), 154104, https://doi.org/10.1063/1.3382344.

[39] A. Dal Corso, Elastic constants of beryllium: a first-principles investigation, J. Phys. Condens. Matter 28 (7) (2016), 075401, https://doi.org/10.1088/0953-8984/28/7/075401.

[40] R. Gaillac, P. Pullumbi, F.-X. Coudert, ELATE: an open-source online application for analysis and visualization of elastic tensors, J. Phys. Condens. Matter 28 (27) (2016), 275201, https://doi.org/10.1088/0953-8984/28/27/275201.

[41] M. Palumbo, A. Dal Corso, Lattice dynamics and thermodynamical properties of h.c. p. Os and Ru from the quasi-harmonic approximation, J. Phys. Condens. Matter 29 (39) (2017), 395401, https://doi.org/10.1088/1361-648x/aa7dca.

[42] A. Togo, I. Tanaka, First principles phonon calculations in materials science, Scripta Mater. 108 (2015) 1–5, https://doi.org/10.1016/j.scriptamat.2015.07.021.

[43] A. Togo, First-principles phonon calculations with phonopy and phono3py, J. Phys. Soc. Jpn. 92 (1) (2023), 012001, https://doi.org/10.7566/jpsj.92.012001.

[44] S.V. Churakov, P. Mandaliev, Structure of the hydrogen bonds and silica defects in the tetrahedral double chain of xonotlite, Cement Concr. Res. 38 (3) (2008) 300–311, https://doi.org/10.1016/j.cemconres.2007.09.014.

[45] N. Demidenko, A. Stetsovskii, Correlation between elastic properties of wollastonite-based materials and sintering temperature, Glass Ceram. 60 (2003).

[46] E. Durgun, H. Manzano, R. Pellenq, J.C. Grossman, Understanding and controlling the reactivity of the calcium silicate phases from first principles, Chem. Mater. 24 (7) (2012) 1262–1267, https://doi.org/10.1021/cm203127m.

[47] V. Swamy, L. Dubrovinsky, Thermodynamic and thermophysical properties of Ca, Mg silicates from Raman spectra, lattice dynamics, and thermodynamic evaluation, Phys. Chem. Miner. 23 (4–5) (1996) 550–561, https://doi.org/10.1007/bf00207772.